Quintic Dispersion Soliton Frequency Combs in a Microresonator

*Shuangyou Zhang, Toby Bi, and Pascal Del'Haye**

Chip-scale optical frequency combs have attracted significant research interest and can be used in applications ranging from precision spectroscopy to telecom channel generators and lidar systems. In the time domain, microresonator based frequency combs correspond to self-stabilized soliton pulses. In two distinct regimes, microresonators are shown to emit either bright solitons in the anomalous dispersion regime or dark solitons (a short time of darkness in a bright background signal) in the normal dispersion regime. Here, the dynamics of continuous-wave-laser-driven soliton generation is investigated in the zero-group-velocity-dispersion regime as well as the generation of solitons that are spectrally crossing different dispersion regimes. In the measurements, zero-dispersion solitons with multipeak structures (soliton molecules) are observed with distinct and predictable spectral envelopes that are a result of fifth-order dispersion of the resonators. Numerical simulations and the analysis of bifurcation structures agree well with the observed soliton states. This is the first observation of soliton generation that is governed by fifth-order dispersion, which can have applications in ultrafast optics, telecom systems, and optical spectroscopy.

1. Introduction

Optical frequency combs based on monolithic high-Q microresonators have been intensively studied over the past 15 years.[1–3] In particular, their chip-scale footprint and low power consumption are of interest for out-of-the-lab applications. The discovery of dissipative Kerr solitons in microresonators enables low-noise, coherent, and broadband frequency combs due to the double balance between the Kerr nonlinearity and group velocity dispersion (GVD) and between the cavity losses and cavity gain.[4] Rich nonlinear physics in microresonators have been revealed in the past decade, including breather solitons,[5,6] soliton crystals,[7,8] Stokes solitons,[9] Pockels solitons,[10] laser cavity solitons,[11] dark solitons,[12,13] and dark-bright soliton pairs.[14] In many of the aforementioned soliton types, the GVD of microresonators plays a critical role in microcomb formation. Solitons in microresonators are separated into two distinct cases, bright solitons (intensity peaks on a low-level background),[4] and dark solitons (intensity dips embedded in a high-intensity background),[12] depending on the second-order resonator dispersion at the pump wavelength. Bright soliton generation in microresonators requires anomalous GVD at the pump wavelength, while dark solitons can be observed when pumping in the normal dispersion regime. Bright solitons can be described to originate from modulation instability,[4] in contrast to dark solitons, which arise through the interlocking of switching waves connecting the homogenous steady-states of the bistable cavity system.[15,16] Recent research theoretically predicted the coexistence of bright and dark solitons in the regimes of normal,[17] zero,[18–20] and anomalous GVD,[21] when taking account of higher-order dispersion (third- and fourth-order).

Among these studies, soliton generation in the zero GVD regime is of particular interest.[22–24] Especially in conventional mode-locked lasers, dispersion compensation with prism pairs and chirped mirrors has been the key to the generation of femtosecond and attosecond pulses. Working in this regime, comb lines from different spectral regions relative to the pump laser (or gain region) experience opposite dispersion, normal dispersion on one side and anomalous dispersion on the other side. As a result, the solitons exhibit asymmetrical behavior both in frequency and time domains. Moreover, working at zero GVD allows us to investigate the higher-order dispersion, which plays a dominant role in the soliton formation dynamics. The bright and dark soliton formation in this regime can also be described by the interlocking of switching waves.[15] Additionally, when pumping close to the zero-dispersion crossing, a dispersive wave (DW) is expected to be generated close to the pump, and hence, soliton formation will be strongly affected by the soliton recoil effect.[18] Zero or small GVD is the key to obtaining spectrally broadband frequency combs, in particular with rapidly growing

S. Zhang, T. Bi, P. Del'Haye
Max Planck Institute for the Science of Light
91058 Erlangen, Germany
E-mail: pascal.delhaye@mpl.mpg.de
T. Bi, P. Del'Haye
Department of Physics
Friedrich-Alexander-Universität Erlangen-Nürnberg
91058 Erlangen, Germany

The ORCID identification number(s) for the author(s) of this article can be found under https://doi.org/10.1002/lpor.202300075

DOI: 10.1002/lpor.202300075

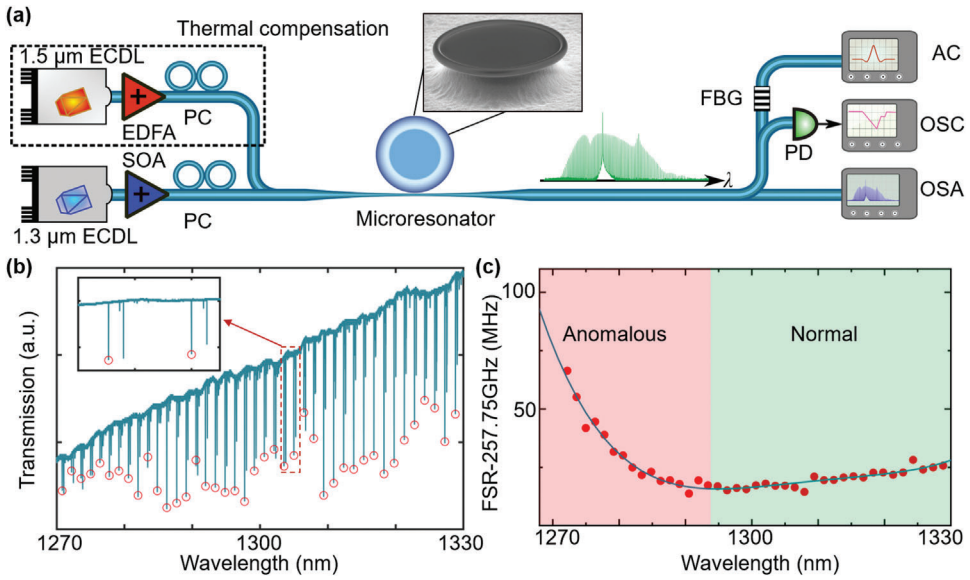

Figure 1. Experimental demonstration of soliton dynamics crossing different dispersion regimes. a) Experimental setup. The 1.3 μm pump laser is used to generate bright solitons by pumping a fused silica microtoroid whose GVD evolves from anomalous to normal within the wavelength range from 1270 to 1330 nm. The 1.5 μm auxiliary laser thermally stabilizes the resonator during the 1.3 μm soliton generation. ECDL: external cavity diode laser; EDFA: erbium-doped fiber amplifier; SOA: semiconductor optical amplifier; PC: polarization controller; PD: photodetector; AC: autocorrelator; OSA: optical spectrum analyzer; OSC: oscilloscope; FBG: fiber Bragg grating. Inset: scanning electron microscope image of the microtoroid used in the experiments. b) Measured mode spectrum of the microtoroid. Inset shows the zoomed-in spectrum around 1304 nm. c) Dispersion of the mode family marked with red circles in (b). Red circles are experimental data while the solid blue trace is a 4th-order polynomial fit, considering up to the fifth-order dispersion.

ways to control microresonator dispersion in waveguide structures. Li et al. recently reported soliton dynamics in a dispersion-managed near-zero net GVD Si_3N_4 microresonators.[24] In addition, Li et al. reported on the first experimental observations of bright soliton generation in a close-to-zero, weakly normal GVD fiber loop resonator.[22] Soon after Anderson et al. demonstrate soliton formation pumping in near zero GVD (weakly normal dispersion) regime in chip-based Si_3N_4 microresonators, resulting in a near octave-spanning spectrum.[23] The zero-GVD solitons observed in these studies are enabled by third-order dispersion (TOD) and both studies use synchronously pulsed-driving of the cavities rather than a continuous wave (CW) laser. However, this synchronously pulsed-driving can be seen as quasi-CW since the generated solitons are much narrower than the driving pulses. Especially in microresonator systems, pulsed pumping can strongly influence the soliton formation process and enables thresholdless comb generation.[25]

In this paper, we demonstrate and explore the soliton dynamics in a microresonator pumped by a CW source in different dispersion regimes ranging from anomalous, crossing zero, to normal GVD. Our studies reveal that the close-to-zero-dispersion solitons in our system are enabled by fifth-order dispersion (5th-OD), a regime that has so far received little attention in the micro-comb community but also in other areas such as ultrafast laser systems and fiber femtosecond lasers. This is in contrast to previous studies,[17,18,22,23] in which zero-dispersion solitons are induced by the TOD. Different zero-dispersion soliton states can be accessed with a predictable spectral profile by adiabatically tuning the laser frequency and pumping different optical modes. To the best of our knowledge, this is the first observation of continuous-wave-pumped zero-GVD soliton molecules in a microresonator, and more importantly, the first report of 5th-OD induced solitons. Our study could stimulate future research in this area with interesting applications in pump probe spectroscopy, telecom systems and optical sensing.

2. Experimental Setup

Figure 1a shows a schematic of the experimental setup. The pump laser at 1.3 μm wavelength is used to generate bright soliton structures to study the soliton dynamics in different GVD regimes. Another laser at 1.5 μm wavelength is used as an auxiliary laser to passively stabilize the circulating optical power within the microresonator to assist soliton generation for the 1.3 μm pump laser.[26] A 250 μm diameter fused silica microtoroid with an free spectral range (FSR) of 257 GHz is used in the experiments and shown in the inset of Figure 1a. This particular microresonator is fabricated from a silicon wafer with a 6 μm layer of thermally grown silicon dioxide (SiO_2).[27] The two lasers are combined with a wavelength division multiplexer (WDM) and evanescently coupled into the microresonator via a tapered optical fiber. Two fiber polarization controllers (PCs) are used to match the polarization of the two lasers to the respective cavity mode polarizations. At the resonator output, the light of the two lasers is separated by another WDM. Part of the 1.3 μm soliton comb light is monitored with an optical spectrum analyzer (OSA) and a photodiode (PD). An autocorrelator (AC) based on second-harmonic generation is used to measure the autocorrelation traces of the 1.3 μm comb light. In addition, a fiber Bragg grating (FBG) filter is used to suppress the pump power before

the AC. In the experiments, the auxiliary laser is used to pump a mode at 1556 nm for the thermal stabilization of the resonator.[26] To mitigate nonlinear interference of the auxiliary laser on the soliton comb, a low-Q optical mode with a large group velocity mismatch relative to the FSR of the pump mode is selected for the auxiliary laser.[28] In addition, the optical power of the auxiliary laser is kept as low as possible, while still being able to passively stabilize the resonator temperature.

The resonance frequencies of a mode family in a whispering-gallery mode resonator made of a dispersive medium can be described as

$$\omega_\mu = \omega_0 + D_1\mu + \frac{D_2}{2!}\mu^2 + \frac{D_3}{3!}\mu^3 + \frac{D_4}{4!}\mu^4 + \frac{D_5}{5!}\mu^5 \quad (1)$$

where μ is the mode number offset from the pump mode at $\mu = 0$ and ω_μ are the resonance frequencies. $D_1/2\pi$ is the FSR of the resonator at the pump mode ($\mu = 0$), and D_2, D_3, D_4, and D_5 are coefficients of second-, third-, fourth-, and fifth-order dispersion, respectively. We employ a high-precision calibrated fiber loop cavity for providing reference frequency markers to measure the mode spectrum of the resonator.[29–31] The FSR (≈40 MHz) of the fiber reference cavity is calibrated with sub-15 Hz frequency precision over a range from 1270 to 1330 nm. This calibration enables a measurement of the ≈250 GHz microresonator FSR with an error of less than 250 GHz/40 MHz × 15 Hz ≈ 90 kHz. Figure 1b shows the measured mode spectrum of the microtoroid used here in the region between 1270 and 1330 nm. There are three different mode families observed in the transmission trace (see Figure S1, Supporting Information). The mode family (red circles) with an intrinsic optical quality factor of 30 million is selected. The GVD of this mode family changes from anomalous to normal. Figure 1c shows the corresponding FSR evolution of the selected soliton mode family. In this measurement, we confirm that the variation of the FSR with respect to the wavelength changes its sign. The GVD of the optical modes shorter than 1294 nm is anomalous (FSR increases with optical frequency), while it becomes normal for wavelengths larger than 1294 nm (FSR decreases with optical frequency). Even though some experimental data points in Figure 1c deviate from the fitted curve, we believe these modes are not related to avoided mode crossings (see Section S1, Supporting Information, for details). In the experiments, the 1.3 µm pump laser is tuned from 1270 to 1304 nm, correspondingly, the GVD of the soliton modes changes from anomalous to normal. Within this range, each longitudinal resonator mode (from the same mode family that is marked with red circles in Figure 1b) supports the formation of a bright soliton, but shows significantly different dynamics due to the variation of the GVD.

3. Bright Soliton Generation with Asymmetric Dispersion

First, we start by pumping a mode at 1283.4 nm in the anomalous GVD regime with a pump power of 55 mW. By optimizing the power and laser-cavity detuning of the 1.5 µm auxiliary laser, 1.3 µm soliton states can be deterministically accessed by manually tuning the 1.3 µm pump laser across its resonance from the blue-detuned side to the red-detuned side.[26] **Figure 2**a shows the measured integrated dispersion profile (blue circles) $D_{\text{int}}(\mu) = \omega_\mu - \omega_0 - \mu D_1$ of this pump mode (1283.4 nm), together with a 5th-order polynomial fit (blue curve). The dispersion trace shows anomalous GVD ($D_2/2\pi$ = 2.1 MHz, $D_3/2\pi$ = 424 kHz, $D_4/2\pi$ = 48.3 kHz, and $D_5/2\pi$ = 2.8 kHz) but also an asymmetric profile on either side of the pump mode. On the left side of the pump wavelength, the dispersion is much stronger than that on the right side, which can be seen from the sharper slope on the left side. As a result, the noncoherent, chaotic spectrum shown in Figure 2b shows a strong asymmetry with a relatively narrow spectrum on the lower wavelength side and a broad spectrum on the higher wavelength side. Subsequently tuning the 1.3 µm pump laser to the red-detuned side of its resonance, a bright single soliton can be generated as shown in Figure 2c, with a sech^2 envelope and a DW at 1388 nm.

In the next step, we further increase the pump wavelength to approach the zero-GVD regime. Figure 2d shows the integrated dispersion measurement (red circles) at the pump wavelength of 1292 nm together with the fitted curve (red). Here, the local dispersion around the pump laser has opposite signs, transitioning from positive values for D_{int} to negative values for increasing wavelengths. The calculated $D_2/2\pi$, $D_3/2\pi$, $D_4/2\pi$, and $D_5/2\pi$ at this pump wavelength are 307.8, 184.2, 31.6, and 2.8 kHz, respectively. Figure 2e,f shows the comb spectra in a chaotic state (Figure 2e) and a single-soliton state (Figure 2f). The single soliton spectrum in Figure 2f has one DW around 1353 nm, which is not phase-matched according to the dispersion profile in Figure 2d. After the soliton formation, the mismatch between the repetition rate and the local FSR creates phase-matching for the DW in Figure 2f. This is attributed to the influence of the dependence of the repetition rate on the soliton recoil, Raman shift, and the laser-cavity detuning[28,32] (see Section S2, Supporting Information, for details). As a result of the soliton recoil effect,[33] the appearance of the DW on the red side of the spectrum causes a blueshift of the central wavelength of the spectral envelope with respect to the pump wavelength. Comparing both spectra in Figure 2c,f, indeed, soliton formation is strongly affected by the soliton recoil effect when pumping close to the zero-dispersion regime.

4. Soliton Generation at Zero GVD

To explore the soliton dynamic in the close-to-zero GVD regime, we tune the pump wavelength to slightly longer wavelengths. **Figure 3**a shows the integrated dispersion measurement at the new pump wavelength of 1303.6 nm together with a fifth-order polynomial fit of the data. The calculated $D_2/2\pi$, $D_3/2\pi$, $D_4/2\pi$, and $D_5/2\pi$ at this pump wavelength are −390.4 kHz (± 21.9 kHz), 19.9 kHz (± 5.1 kHz), 9.5 kHz (± 0.9 kHz), and 2.8 kHz (± 0.2 kHz), respectively. When the pump laser approaches the zero-GVD regime, the dispersion close to the pump mode becomes flatter compared to Figure 2a,d. Figure 3b shows a transmission trace when slowly scanning the 1.3 µm pump laser (at ≈1 GHz s^{-1}) across the resonance from the blue- to the red-detuned side while simultaneously coupling the 1.5 µm auxiliary laser into its resonance for thermal compensation. On the blue-detuned side of the soliton resonance (left side of the dashed line), the comb is in a noncoherent chaotic state and the corresponding

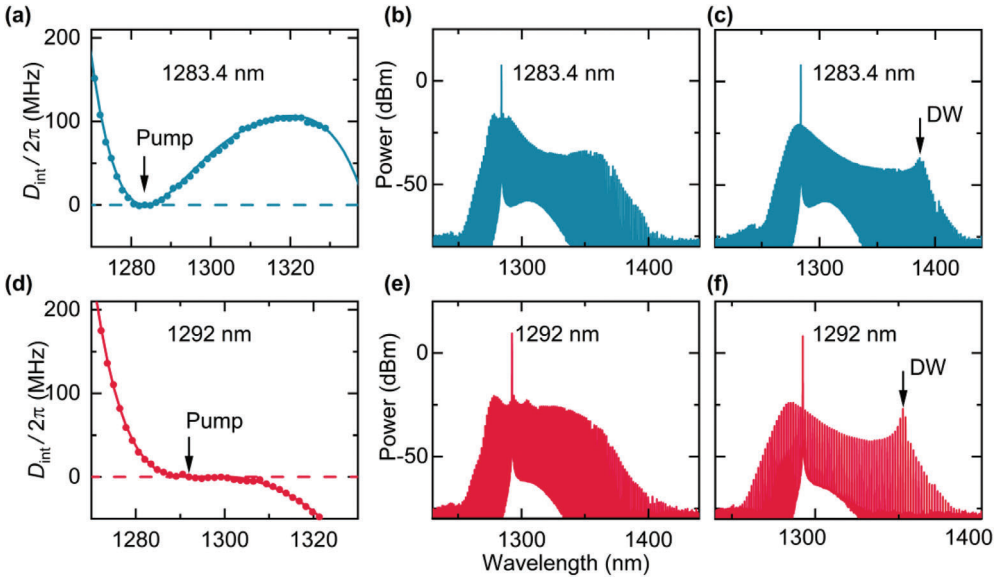

Figure 2. Bright soliton generation with asymmetric dispersion. a) Measured integrated dispersion profile (blue circles) at pump wavelength of 1283.4 nm together with a polynomial fit (solid trace). Optical spectrum when the microcomb is in b) a chaotic and c) single-soliton state. d) Measured integrated dispersion profile (red circles) at pump wavelength of 1292 nm together with a polynomial fit (solid trace). Optical spectrum when the microcomb is in e) a chaotic and f) single-soliton state.

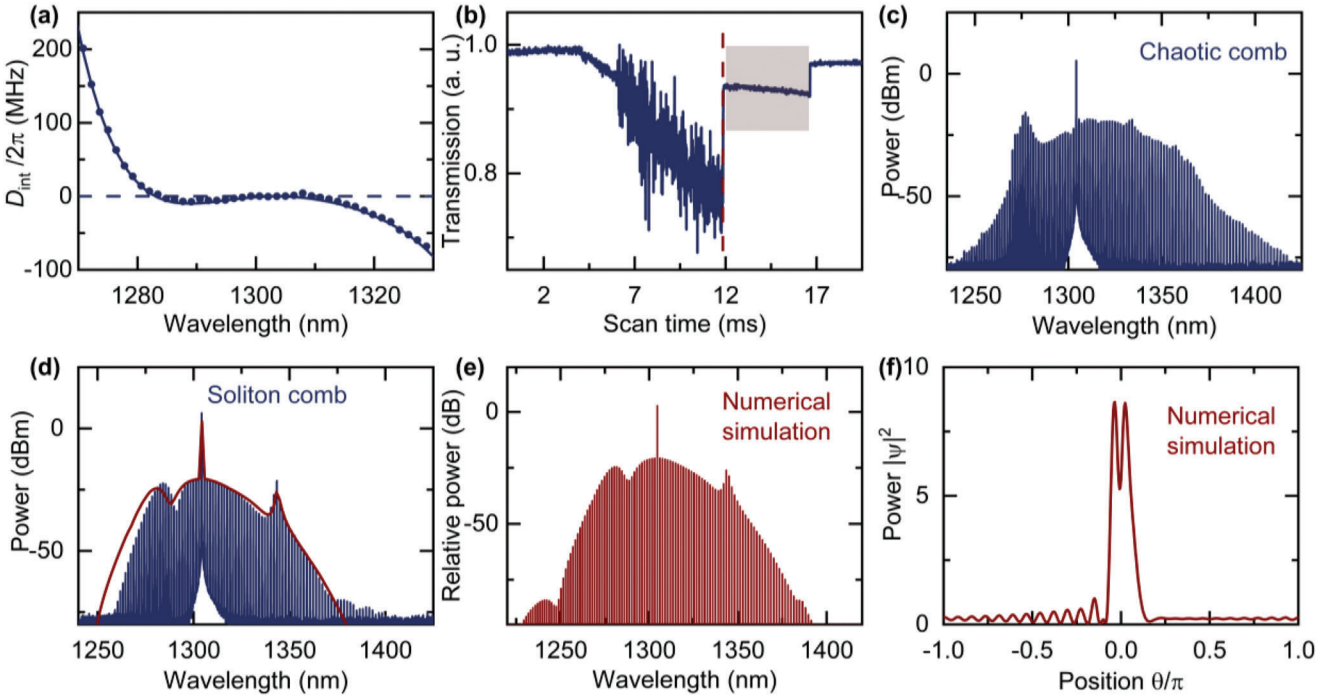

Figure 3. Measurement of a zero-GVD soliton in a microresonator driven by a continuous wave laser. a) Integrated dispersion measured at 1303.6 nm. b) Measured transmission trace when scanning the 1.3 μm pump laser frequency from the blue-detuned to the red-detuned side of the resonance. c) Measured spectrum when the microcomb is in a chaotic state. d) Measured spectrum of a soliton state overlaid with a simulated spectral envelope in red. e) Numerically simulated optical spectrum and the corresponding intracavity temporal waveform. f) $|\psi|^2$ is the dimensionless intracavity power.

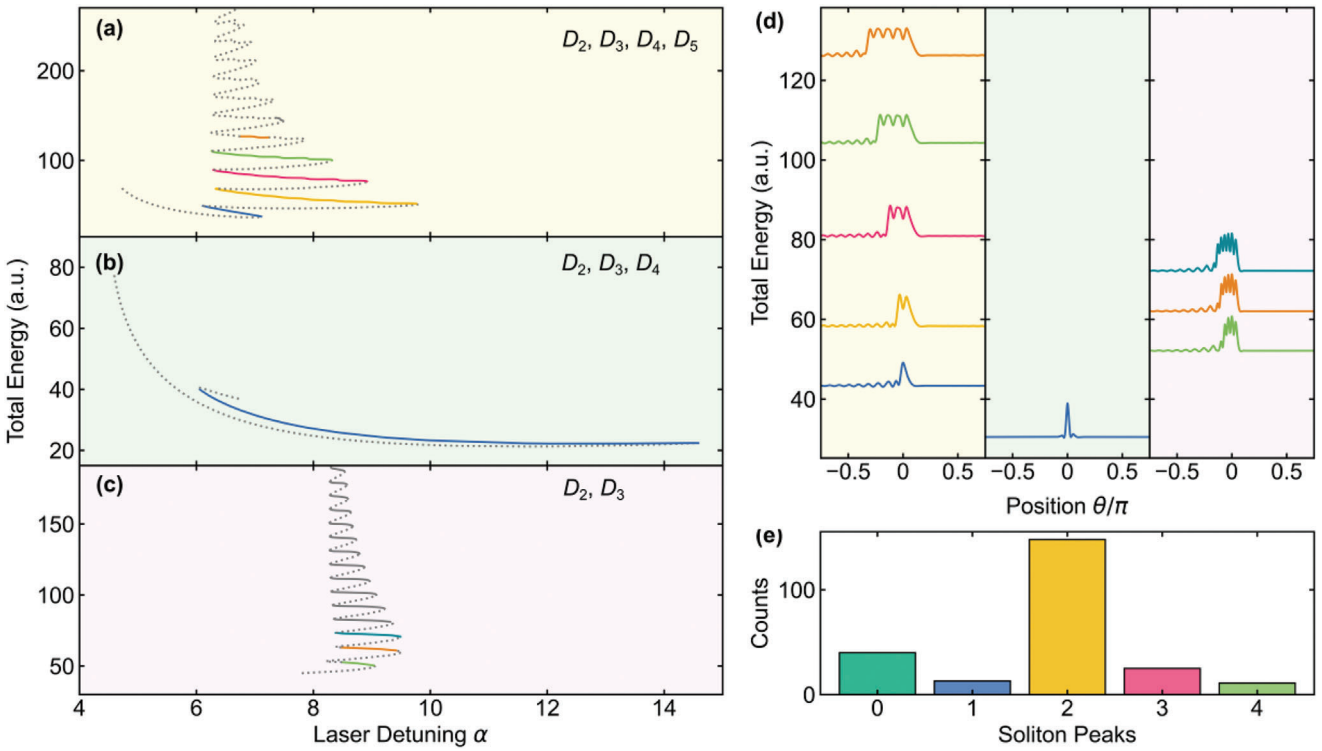

Figure 4. Numerically simulated snaking bifurcation structure under different dispersion parameters as a function of laser detuning α (normalized to half of a cavity linewidth). a) Simulation with dispersion parameters of $D_2/2\pi$, $D_3/2\pi$, $D_4/2\pi$, and $D_5/2\pi$ of −390.4, 19.9, 9.5, and 2.8 kHz. b) Simulation with dispersion parameters of $D_2/2\pi$, $D_3/2\pi$, and $D_4/2\pi$, of −390.4, 19.9, and 9.5 kHz. c) Simulation with dispersion parameters of $D_2/2\pi$, and $D_3/2\pi$ of −390.4 and 25.3 kHz. Note that the D_3 used for this simulation is higher than the experimentally measured value due to the difficulty in obtaining stable bright-soliton structures at lower TOD. d) Corresponding stable bright-soliton temporal profiles of (a)–(c) offset by the total energy in the cavity. e) Histogram of peak numbers of numerically simulated solitons when sweeping the laser detuning using the dispersion parameters from panel (a).

spectrum is shown in Figure 3c. Note that, even though under normal dispersion, the field experiences modulation instability gain, which is enabled by the fourth-order dispersion (4th-OD) of our system. The 4th-OD has an opposite sign compared to the second-order dispersion, making the phase-matching condition possible for four-wave mixing.[34–37] This enables the generation of bright solitons in the normal dispersion regime with an adiabatic laser detuning scan. As expected from Figure 3a, the spectrum becomes more symmetric with respect to the pump laser, in comparison to the spectra in Figure 2b,e. We can still observe a distinct DW at 1277 nm.

When tuning the pump laser frequency into the soliton step (shaded area in Figure 3b), a bright soliton is formed with a significantly smoother spectral envelope compared to the chaotic spectrum in Figure 3c. Figure 3d shows the optical spectrum of this bright zero-GVD soliton. Interestingly, the soliton spectrum has a distinct envelope with a spectral dip on the blue-detuned side of the pump and a DW on the red-detuned side. The distinct envelope is different from those of conventional bright (sech^2 envelope) and dark solitons. To investigate the intracavity dynamics of the zero-GVD soliton, a number of numerical simulations are performed based on a generalized mean-field Lugiato–Lefever equation (LLE),[38–40] taking into account up to 5th-OD (see the Experimental Section for details about the numerical model). Figure 3e,f shows the numerically simulated optical spectrum and the corresponding intracavity temporal waveform, respectively. The simulated spectra are in excellent agreement with the measurements. The intracavity temporal waveform in Figure 3f reveals a two-peak bright soliton with a DW-induced oscillation in the pedestals.

Theoretical studies predicted that TOD can enable the coexistence of dark and bright solitons under normal dispersion.[17,18] Recent works have demonstrated that zero-GVD solitons with multiple peaks are induced by TOD.[22,23] In contrast, even with the maximum possible value ($D_3/2\pi$ = 25 kHz) from the polynomial fitting uncertainty, the TOD in our system is too weak to support bright solitons or multipeak bright solitons. To verify the dominant effect of 5th-OD, we theoretically investigate the bifurcation structure and stability of the soliton states in our system. By solving the steady-state solutions of the LLE using a Newton–Raphson continuation algorithm,[39] **Figure 4** shows three collapsed snaking bifurcation structures[17,22] under different dispersion configurations (see the Numerical Methods section at the end of the paper for details about the Newton–Raphson continuation algorithm). Figure 4a presents the snaking bifurcation structure of the energy of bright solitons[17] as a function of laser detuning with dispersion parameters of $D_2/2\pi = -390.4$ kHz, $D_3/2\pi = 19.9$ kHz, $D_4/2\pi = 9.5$ kHz, and $D_5/2\pi = 2.8$ kHz, where several different stable soliton solutions (solid trace) coexist in the system and each solid line at different energy levels corresponds to different bright soliton states with different peak numbers in the temporal profile, as shown in the

first column of Figure 4d. The detuning range of two-, three-, and four-peak solitons is relatively large, while those of other soliton states are narrow. However, we also observe single-peak solitons in the simulation, suggesting that the two-peak soliton in Figure 3 can be understood as two solitons that are bound together, which can also be referred to as a soliton molecule.[41,42] In this case, the binding mechanism is determined by the 5th-OD of the resonator. On the other hand, the measured two-peak soliton can be possibly explained as interlocked switching waves, where the upswitching wave has two peaks on the high-intensity solution induced by 5th-OD. Note that, with the particular pump wavelength used in this measurement, accessing a single-peak soliton is experimentally challenging due to the relatively narrow detuning range of its existence, as shown in Figure 4a.

In comparison, Figure 4b,c shows the bifurcation diagram with dispersion parameters of $D_2/2\pi = -390.4$ kHz, $D_3/2\pi = 19.9$ kHz, $D_4/2\pi = 9.5$ kHz, and $D_5/2\pi = 0$ kHz for (b) and $D_2/2\pi = -390.4$ kHz, $D_3/2\pi = 25.3$ kHz, $D_4/2\pi = 0$ kHz, and $D_5/2\pi = 0$ kHz for (c), respectively. Figure 4b shows the bifurcation diagram in the presence of second-, third-, and fourth-order dispersion. Without 5th-OD, there is only one bright soliton solution in the system, with a temporal profile shown in the middle column of Figure 4d. As discussed above, the 4th-OD in our system enables the generation of bright solitons by inducing phase-matching for four-wave mixing in the zero GVD region. However, it is not responsible for the observed zero-GVD solitons. Figure 4c shows the bifurcation diagram under the impact of only D_2 and D_3. Please note that under normal dispersion, the existence range of bright solitons increases with the value of D_3.[17] In our system, the experimental value $D_3/2\pi$ is weak (19.9 kHz, corresponding to −0.17 in dimensionless units[17]) and hinders the numerical simulation from finding the stable solutions. To illustrate the effect of TOD on the bifurcation structure, we increase $D_3/2\pi$ to 25.3 kHz, corresponding to a dimensionless TOD of −0.22. As shown in Figure 4c, there are several stable solutions of bright solitons with different peak numbers coexisting in the system, whose temporal profiles are plotted in the third column of Figure 4d. However, there are no stable single-, two- and three-peak solitons. The first stable bright soliton in the system is a four-peak soliton with an existence range of only 25% of a resonance linewidth. With the bifurcation results in Figure 4, we conclude that the existence range of multipeak solitons is greatly extended by the 5th-OD, and therefore, the zero-dispersion solitons observed here are enabled by 5th-OD. The same simulation results are observed when modifying the 5th-OD $D_5/2\pi$ within the error margin of the polynomial fitting (see Supporting Information for details on the impact of TOD, 4th-OD, and 5th-OD).

Figure 4a suggests that multipeak soliton states with different temporal and spectral profiles can coexist under the same system parameters with the influence of the 5th-OD (see first column in Figure 4d and the Supporting Information for details). However, apart from the two-peak soliton in Figure 3, other multipeak soliton states are not observed in our experiments when adiabatically scanning the laser detuning. The reason is that the existence range of the two-peak solitons is larger than that of other multipeak soliton states. When slowly changing the laser frequency from the blue- to the red-detuned side of the resonance, the intracavity field experiences intense and random chaotic states, and the spontaneous formation of bright soliton structures tend to be the state with the highest probability (two-peak soliton in our case). To further verify the two-peak soliton as the highest probability state, Figure 4e shows the histogram of peak numbers of the generated soliton states when repeatedly running a split-step LLE simulation by scanning the laser frequency across the cavity resonance using the same parameters as used in Figure 3. Here, the LLE simulation does not include thermally induced resonance shifts and instabilities of the microresonator. The thermal instabilities as well as modulational instability make it challenging to observe multisoliton states with more than two peaks in the experiments. However, with more advanced experimental methods, such as actively locking the laser detuning, we believe that different soliton states could be accessible.[22] Note that, once generated, the zero-GVD solitons demonstrated in this work are stable and sustain their shape within a large cavity-pump detuning range (see the Supporting Information for details).

The results presented above demonstrate that zero-GVD solitons at a specific pump mode can be generated with a predictable profile and sustain its shape regardless of cavity-pump detuning variation. Here, we highlight that several types of zero-GVD solitons with different temporal and spectral profiles can be accessed by pumping different optical modes. **Figure 5**a shows two measurements of the transmission signal when scanning the 1.3 μm pump laser across a resonance at 1299.2 nm, with dispersion parameters of $D_2/2\pi = -275.8$ kHz, $D_3/2\pi = 60.7$ kHz, $D_4/2\pi = 17.8$ kHz, and $D_5/2\pi = 2.8$ kHz. In the red-detuned regime (right side of the vertical dashed line), we observe two different soliton steps. Figure 5b shows an experimental spectrum of a bright soliton when the microcomb is in the lower soliton step (yellow area in Figure 5a). It is interesting to note that, in contrast to the experimental spectra in Figure 3, there is another spectral dip on the longer-wavelength side of the pump, in addition to the one on the shorter-wavelength side. Similar to Figure 3, there is also a DW on the longer-wavelength side of the pump laser. Figure 5c shows the numerically simulated spectrum, which agrees well with the measured spectrum in Figure 5b. Figure 5d shows the simulated intracavity temporal waveform corresponding to the spectrum in Figure 5c, which suggests that the experimental result in Figure 5b corresponds to a bright doublet soliton in the time domain. To further verify the temporal profile, we measure the autocorrelation traces by sending the light with the spectrum from Figure 5b into an autocorrelator. An FBG filter is used to suppress the pump laser and a semiconductor optical amplifier amplifies the comb signal before sending the light into the autocorrelator. The filtered and amplified comb spectrum is presented in the Supporting Information. Figure 5e shows the normalized autocorrelation trace (blue) of the two-peak soliton. The two sidelobes are associated with the doublet structure shown in Figure 5d. The temporal separation of the sidelobes is larger compared to the calculated result (red trace in Figure 5e) based on the temporal waveform in Figure 5d. This mismatch originates from the distortion by the SOA amplifier, as well as fiber dispersion and the used FBG filter. Compared with Figure 3f, the temporal delay between the two peaks in Figure 5d is larger, further suggesting that the two-peak soliton demonstrated here can be considered as a soliton molecule, where two individual solitons are bound together. In fact, when pumping this mode, a single isolated bright soliton can also be accessed experimentally. The existence range of the single-peak

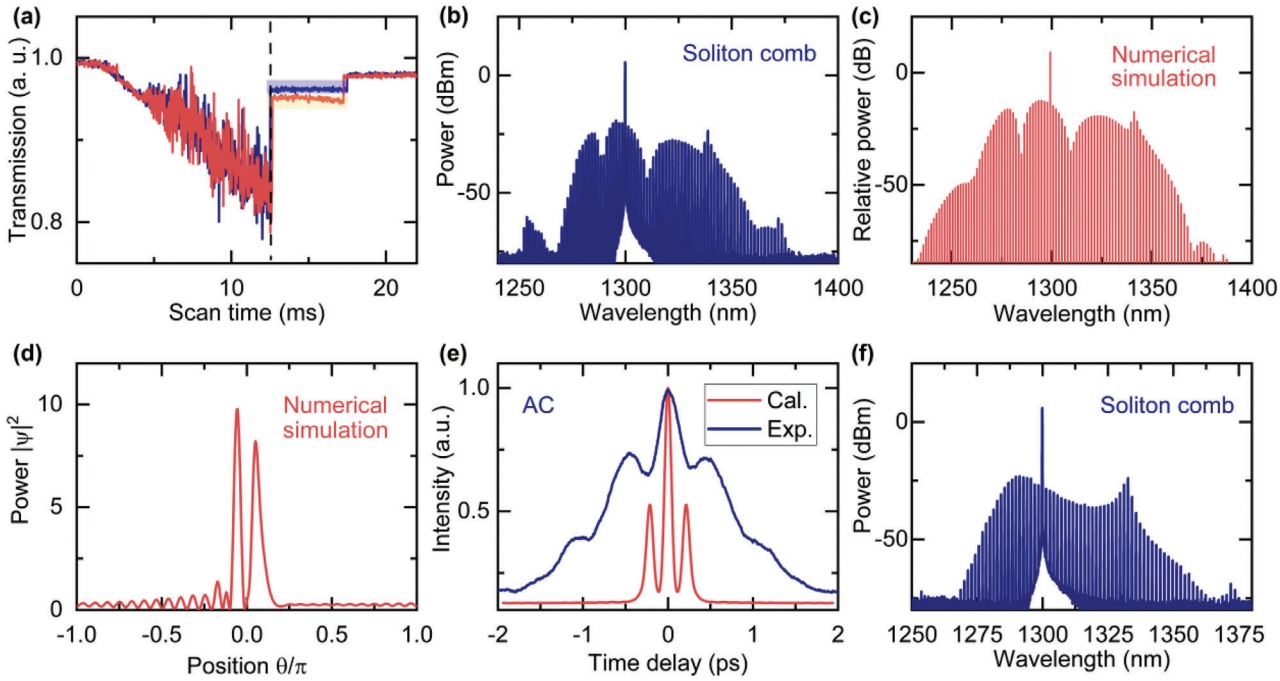

Figure 5. Measurement of different zero-GVD solitons driven at different microresonator modes. a) Experimental transmission traces when scanning the 1.3 μm pump laser frequency across its resonance from the blue- to the red-detuned side. The right side of the dashed line shows two steps (marked with blue and red shaded background) corresponding to two different soliton states. b) Measured spectrum of a zero-GVD soliton at 1299.2 nm. c) Numerically simulated intracavity optical spectrum and the corresponding temporal waveform (d). e) Measured autocorrelation trace (blue) of the zero-GVD soliton with the spectrum shown in (b) after propagation through an amplifier and several meters of optical fiber, together with a calculated trace (red) based on temporal waveform in (d). f) Spectrum of a single isolated bright soliton in the zero-GVD regime.

soliton at this pump mode is extended due to different dispersion parameters, compared to the parameters used in Figure 3. The corresponding spectrum is shown in Figure 5f when the microcomb is in the upper soliton step (blue area) in Figure 5a.

5. Conclusion

In conclusion, we explored microresonator soliton dynamics in the zero-GVD regime and in the transition range between anomalous and normal dispersion, driven by a continuous wave laser. Numerical simulation and investigations of bifurcation structure reveal that the observed zero-GVD solitons are enabled by fifth-order dispersion. This is the first demonstration of soliton formation induced by fifth-order dispersion. Multipeak soliton structures can be accessed with a stable temporal profile when pumping optical modes close-to-zero GVD. The shape and temporal delay of the zero-GVD solitons can be controlled by changing the pump modes. These results could be used for new types of chip-integrated pump-probe experiments. In particular, the rapid advances in photonic integration and emerging techniques of inverse photonic design and machine learning,[43–45] more complex and specially tailored dispersion profiles can be realized. This dispersion control enables further studies on the soliton dynamics induced by higher-order dispersion in these systems. A precise understanding of the soliton dynamics is important for optical frequency comb generation in microresonators with applications in precision spectroscopy, attosecond science, optical telecommunication systems,[40] and chip-integrated lidar systems.

Note added: we would like to draw the reader's attention to two related recent works[46,47] that were published during the review process.

6. Numerical Methods

6.1. Numerical Simulations

To simulate the temporal dynamics of the formation of zero-dispersion solitons in a microresonator, a generalized LLE was solved[40,48]

$$\frac{\partial \psi(\theta,\tau)}{\partial \tau} = -(1+i\alpha)\psi + i|\psi|^2\psi - \sum_{n=2}^{n\geq 2}(-i)^{n+1}\frac{\beta_n}{n!}\frac{\partial^n \psi}{\partial \theta^n} + F \quad (2)$$

where τ is the slow time, normalized to twice the photon lifetime (τ_{ph}) and θ is the azimuthal angle in a frame corotating at the group velocity. $\psi(\theta,\tau)$ is the intracavity field envelope. α is the frequency detuning of the pump laser (angular frequency ω_p) with respect to the resonance frequency (angular frequency ω_0) and normalized to the half-width at half-maximum of the resonance $\Delta\omega_0$

$$\alpha = -\frac{\omega_p - \omega_0}{\Delta\omega_0/2} \quad (3)$$

β_n are the nth-order dimensionless dispersion coefficients at the primary pump mode, normalized as $\beta_n = -2D_n/\Delta\omega_0$. The con-

stant F is the dimensionless external pump amplitude,[48] normalized as

$$F = \sqrt{\frac{8g_0\Delta\omega_{ext}}{\Delta_0^3}\frac{P}{\hbar\omega_p}} \tag{4}$$

where P is the input optical power in watts and $\Delta\omega_{ext}$ is the coupling linewidth. The nonlinear gain g_0 is given as

$$g_0 = \frac{n_2 c\hbar{\omega_p}^2}{n_0^2 V_0} \tag{5}$$

where n_2 and n_0 are the nonlinear (second-order) and linear indices of refraction, respectively, c is the vacuum speed of light and, V_0 is the effective nonlinear mode volume. The LLE simulations are solved numerically using the split-step Fourier and the Newton-Rapson method.

6.2. Newton–Raphson Continuation Algorithm

In Figure 4a–c, the existence detuning range of different peak solitons is calculated using a Newton-Rapson continuation algorithm. The search was initialized using a stable soliton solution of the LLE which was numerically calculated with the split-step Fourier method. Using the Newton-Rapson method, the system approached a stationary solution and the stability was evaluated at this specific detuning. For the next search at a slightly different detuning, the previous solved solution was used as the initial guess and the system stability is evaluated. This was repeated until all the connected stationary solutions were found in the parameter space of interest. For this simulation, the system was initialized in the soliton regime with a stable soliton solution. The detuning was slightly changed within the red-detuned regime between different search rounds. Figure 4a–d in the main text shows the theoretically possible solutions in the system and their respective detuning existence ranges.

Supporting Information

Supporting Information is available from the Wiley Online Library or from the author.

Acknowledgements

This work was supported by the European Union's H2020 European Research Council Starting Grant "CounterLight" 756966, H2020 Marie Sklodowska-Curie COFUND "Multiply" 713694, Marie Curie Innovative Training Network "Microcombs" 812818, and the Max Planck Society.

Open access funding enabled and organized by Projekt DEAL.

Conflict of Interest

The authors declare that they have no conflict of interest.

Data Availability Statement

The data that support the findings of this study are available from the corresponding author upon reasonable request.

Keywords

frequency comb, high-order dispersion, quintic dispersion, soliton

Received: January 26, 2023
Revised: April 6, 2023
Published online: May 12, 2023

[1] P. Del'Haye, A. Schliesser, O. Arcizet, T. Wilken, R. Holzwarth, T. J. Kippenberg, *Nature* **2007**, *450*, 1214.
[2] T. J. Kippenberg, A. L. Gaeta, M. Lipson, M. L. Gorodetsky, *Science* **2018**, *361*, eaan8083.
[3] B. Stern, X. Ji, Y. Okawachi, A. L. Gaeta, M. Lipson, *Nature* **2018**, *562*, 401.
[4] T. Herr, V. Brasch, J. D. Jost, C. Y. Wang, N. M. Kondratiev, M. L. Gorodetsky, T. J. Kippenberg, *Nat. Photonics* **2014**, *8*, 145.
[5] M. Yu, J. K. Jang, Y. Okawachi, A. G. Griffith, K. Luke, S. A. Miller, X. Ji, M. Lipson, A. L. Gaeta, *Nat. Commun.* **2017**, *8*, 14569.
[6] E. Lucas, M. Karpov, H. Guo, M. L. Gorodetsky, T. J. Kippenberg, *Nat. Commun.* **2017**, *8*, 736.
[7] D. C. Cole, E. S. Lamb, P. Del'Haye, S. A. Diddams, S. B. Papp, *Nat. Photonics* **2017**, *11*, 671.
[8] M. Karpov, M. H. P. Pfeiffer, H. Guo, W. Weng, J. Liu, T. J. Kippenberg, *Nat. Phys.* **2019**, *15*, 1071.
[9] Q.-F. Yang, X. Yi, K. Y. Yang, K. Vahala, *Nat. Phys.* **2017**, *13*, 53.
[10] A. W. Bruch, X. Liu, Z. Gong, J. B. Surya, M. Li, C.-L. Zou, H. X. Tang, *Nat. Photonics* **2021**, *15*, 21.
[11] H. Bao, A. Cooper, M. Rowley, L. Di Lauro, J. S. Totero Gongora, S. T. Chu, B. E. Little, G.-L. Oppo, R. Morandotti, D. J. Moss, B. Wetzel, M. Peccianti, A. Pasquazi, *Nat. Photonics* **2019**, *13*, 384.
[12] X. Xue, Y. Xuan, Y. Liu, P.-H. Wang, S. Chen, J. Wang, D. E. Leaird, M. Qi, A. M. Weiner, *Nat. Photonics* **2015**, *9*, 594.
[13] E. Nazemosadat, A. Fülöp, Ó. B. Helgason, P.-H. Wang, Y. Xuan, D. E. Leaird, M. Qi, E. Silvestre, A. M. Weiner, V. Torres-Company, *Phys. Rev. A* **2021**, *103*, 013513.
[14] S. Zhang, T. Bi, G. N. Ghalanos, N. P. Moroney, L. Del Bino, P. Del'Haye, *Phys. Rev. Lett.* **2022**, *128*, 033901.
[15] P. Parra-Rivas, D. Gomila, E. Knobloch, S. Coen, L. Gelens, *Opt. Lett.* **2016**, *41*, 2402.
[16] G. N. Campbell, S. Zhang, L. Del Bino, P. Del'Haye, G.-L. Oppo, *Phys. Rev. A* **2022**, *106*, 043507.
[17] P. Parra-Rivas, D. Gomila, L. Gelens, *Phys. Rev. A* **2017**, *95*, 053863.
[18] J. H. Talla Mbé, C. Milián, Y. K. Chembo, *Eur. Phys. J. D* **2017**, *71*, 196.
[19] C. Bao, H. Taheri, L. Zhang, A. Matsko, Y. Yan, P. Liao, L. Maleki, A. E. Willner, *J. Opt. Soc. Am. B* **2017**, *34*, 715.
[20] S. Yao, K. Liu, C. Yang, *Opt. Express* **2021**, *29*, 8312.
[21] J. H. T. Mbé, Y. K. Chembo, *J. Opt. Soc. Am. B* **2020**, *37*, A69.
[22] Z. Li, Y. Xu, S. Coen, S. G. Murdoch, M. Erkintalo, *Optica* **2020**, *7*, 1195.
[23] M. H. Anderson, W. Weng, G. Lihachev, A. Tikan, J. Liu, T. J. Kippenberg, *Nat. Commun.* **2022**, *13*, 4764.
[24] Y. Li, S.-W. Huang, B. Li, H. Liu, J. Yang, A. K. Vinod, K. Wang, M. Yu, D.-L. Kwong, H.-T. Wang, K. K.-Y. Wong, C. W. Wong, *Light: Sci. Appl.* **2020**, *9*, 52.
[25] D. V. Strekalov, N. Yu, *Phys. Rev. A* **2009**, *79*, 041805.
[26] S. Zhang, J. M. Silver, L. D. Bino, F. Copie, M. T. M. Woodley, G. N. Ghalanos, A. Ø. Svela, N. Moroney, P. Del'Haye, *Optica* **2019**, *6*, 206.
[27] S. Zhang, J. M. Silver, X. Shang, L. D. Bino, N. M. Ridler, P. Del'Haye, *Opt. Express* **2019**, *27*, 35257.
[28] S. Zhang, J. M. Silver, T. Bi, P. Del'Haye, *Nat. Commun.* **2020**, *11*, 6384.
[29] S. Fujii, T. Tanabe, *Nanophotonics* **2020**, *9*, 1087.

[30] X. Zhang, G. Lin, T. Sun, Q. Song, G. Xiao, H. Luo, *Photonics Res.* **2021**, *9*, 2222.
[31] S. Zhang, T. Bi, P. Del'Haye, **2023**, https://doi.org/10.48550/arXiv.2303.14180.
[32] X. Yi, Q.-F. Yang, X. Zhang, K. Y. Yang, X. Li, K. Vahala, *Nat. Commun.* **2017**, *8*, 14869.
[33] M. Karpov, H. Guo, A. Kordts, V. Brasch, M. H. P. Pfeiffer, M. Zervas, M. Geiselmann, T. J. Kippenberg, *Phys. Rev. Lett.* **2016**, *116*, 103902.
[34] N. L. B. Sayson, T. Bi, V. Ng, H. Pham, L. S. Trainor, H. G. L. Schwefel, S. Coen, M. Erkintalo, S. G. Murdoch, *Nat. Photonics* **2019**, *13*, 701.
[35] S. Fujii, S. Tanaka, M. Fuchida, H. Amano, Y. Hayama, R. Suzuki, Y. Kakinuma, T. Tanabe, *Opt. Lett.* **2019**, *44*, 3146.
[36] N. L. B. Sayson, K. E. Webb, S. Coen, M. Erkintalo, S. G. Murdoch, *Opt. Lett.* **2017**, *42*, 5190.
[37] X. Lu, G. Moille, A. Singh, Q. Li, D. A. Westly, A. Rao, S.-P. Yu, T. C. Briles, S. B. Papp, K. Srinivasan, *Optica* **2019**, *6*, 1535.
[38] L. A. Lugiato, R. Lefever, *Phys. Rev. Lett.* **1987**, *58*, 2209.
[39] S. Coen, H. G. Randle, T. Sylvestre, M. Erkintalo, *Opt. Lett.* **2013**, *38*, 37.
[40] Y. K. Chembo, C. R. Menyuk, *Phys. Rev. A* **2013**, *87*, 053852.
[41] L. F. Mollenauer, R. H. Stolen, J. P. Gordon, *Phys. Rev. Lett.* **1980**, *45*, 1095.
[42] P. Rohrmann, A. Hause, F. Mitschke, *Phys. Rev. A* **2013**, *87*, 043834.
[43] G. H. Ahn, K. Y. Yang, R. Trivedi, A. D. White, L. Su, J. Skarda, J. Vučković, *ACS Photonics* **2022**, *9*, 1875.
[44] C. Zhang, G. Kang, J. Wang, Y. Pan, J. Qu, *Opt. Express* **2022**, *30*, 44395.
[45] A. Pal, A. Ghosh, S. Zhang, T. Bi, P. Del'Haye, *Opt. Express* **2023**, *31*, 8020.
[46] Q.-X. Ji, W. Jin, L. Wu, Y. Yu, Z. Yuan, W. Zhang, M. Gao, B. Li, H. Wang, C. Xiang, J. Guo, A. Feshali, M. Paniccia, V. S. Ilchenko, A. B. Matsko, J. E. Bowers, K. J. Vahala, *Optica* **2023**, *10*, 279.
[47] Z. Xiao, T. Li, M. Cai, H. Zhang, Y. Huang, C. Li, B. Yao, K. Wu, J. Chen, *Light: Sci. Appl.* **2023**, *12*, 33.
[48] C. Godey, I. V. Balakireva, A. Coillet, Y. K. Chembo, *Phys. Rev. A* **2014**, *89*, 063814.